Laser and Particle Beams (1997), *vol.* 15, *no.* 1, *pp.* 197–211
Printed in the United States of America

Simulation of relativistic electron generation in under-dense laser plasma experiments

By G. MANFREDI, R. BINGHAM, AND R.O. DENDY
Rutherford Appleton Laboratory, Chilton, Didcot, Oxon, OX11 0QX, United Kingdom

(Received 1 August 1995; Revised 21 May 1996; Accepted 9 June 1996)

The generation of relativistic electrons by nonlinear coupling of a laser beam to an under-dense plasma is simulated. An Eulerian Vlasov code is used, which enables direct solution of the fully nonlinear Vlasov–Maxwell system in real space. The impact of stimulated Raman and Compton scattering on the electron velocity distribution is investigated. Simulations show that electrons can be accelerated to energies of several MeV. The role of induced scattering processes is analyzed in detail, using electromagnetic field spectra and electron phase-space information as diagnostics. The effects of density gradients in the background plasma are also quantified.

1. Introduction

One of the most topical aspects of laser–plasma interactions is the production of energetic electrons in laser-driven plasma accelerators (Joshi *et al.* 1984) and in laser fusion experiments (Kruer 1988). In laser–plasma acceleration experiments at low density, measurements of MeV electrons have been made (Joshi *et al.* 1984; Modena *et al.* 1995), and attributed to resonant acceleration by large amplitude Langmuir waves nonlinearly excited by the laser beams. In laser fusion, considerable attention has focused on indirect drive schemes, where the laser beams ablate the inside wall of a hohlraum creating a hot plasma. Fusion hohlraums are irradiated first with relatively long duration laser pulses and therefore fill with large (~ a few mm) under-dense plasmas with densities $n_e \sim 0.1 n_{cr}$, where n_{cr} is the critical density at which the plasma frequency would equal the laser frequency, and temperatures in the keV range (Tabak *et al.* 1994). During this phase, parametric instabilities can occur, in particular stimulated Raman instabilities, producing waves that may accelerate energetic electrons (Decker *et al.* 1994). To simulate wave excitation and electron acceleration in these scenarios, the combined effect of three types of instability is studied here using the 1D Eulerian Vlasov code developed by Ghizzo and Bertrand (Ghizzo *et al.* 1993; Bertrand *et al.* 1994). These instabilities are stimulated Raman backscattering (SRBS) (Offenberger *et al.* 1982) and forwardscattering (SRFS) (Kruer 1988; McKinstrie & Bingham 1992), which are both resonant processes, and stimulated Compton scattering (SCS), which is a nonresonant process (Lin & Dawson 1975).

In 1D SRBS, the Langmuir wave has a wave number k_p equal to the sum of the incident laser wave number k_o and the wave number of the stimulated backscatter electromagnetic wave k_s such that $k_p = |k_o| + |k_s|$. This Langmuir wave, which has a phase velocity much less than the speed of light, propagates in the same direction as the incident laser beam and can accelerate thermal electrons to higher velocities.

For plasma temperatures of several keV, the Debye length is sufficiently large that the plasma wave associated with SRBS has a wave number such that $k_p \lambda_{De} \simeq O(1)$. In consequence, Landau damping starts to play a crucial role, and such a wave can no longer

 0263-0346/97 $11.00 + .10

develop as a normal mode of the plasma. However, part of the energy of the incident laser beam can be directly transferred to the background electrons as incoherent thermal motion, thus producing a suprathermal tail in the electron distribution function. This process is known as stimulated Compton scattering. We also note that a similar process, the decay of SRBS into SCS via plasma wave breaking, has been the subject of recent experimental studies (Everett *et al.* 1995).

In SRFS, the incident laser beam couples to a high-phase velocity plasma wave producing an upshifted anti-Stokes ($k_{AS} = k_o + k_p$) electromagnetic wave and a down-shifted Stokes ($k_S = k_o - k_p$) electromagnetic wave. All waves in SRFS travel in the same direction, namely that of the incident laser beam. In an underdense plasma ($\omega_o \gg \omega_{pe}$, where ω_{pe} is the electron plasma frequency), the plasma wave generated by SRFS has a phase velocity that is close to, but less than, the speed of light ($v_{ph} \leq c$). This wave is responsible for the resonant acceleration to MeV energies of the nonthermal electrons already accelerated from the thermal background, for example, by the SCS process. These MeV electrons can be used as a diagnostic of the Raman processes described above, as well as generating high-energy X-ray and γ-ray signatures. They could also cause photoneutron production in surrounding materials, via bremsstrahlung.

In this paper, we simulate the acceleration of electrons to relativistic velocities, using the 1D Eulerian Vlasov code of Ghizzo *et al.* (1993), which is described in more detail in the Appendix. In section 2, we describe the physical model adopted here and discuss the assumptions leading to our equations. The main results are presented in section 3: for plasma parameters that are broadly comparable to those of laser fusion experiments, we observe the production of highly energetic electrons, up to 7 MeV. The role of Raman and Compton instabilities is investigated through the analysis of the electron motion in phase space, and the spectra of the electromagnetic fields. A second important issue, namely the presence of a small gradient in the plasma density, is analyzed at the end of section 3: it is shown that a smaller fraction of electrons is accelerated to high energies.

2. Model and numerical code

We consider a linearly polarized electromagnetic wave propagating along the x direction, described by the electric field E_y and the magnetic field B_z. The wave interacts with a plasma, in which all quantities are taken to be functions of the longitudinal coordinate x and of time only. In our 1D model, the electron plasma is described by the relativistic Vlasov equation for $f(x, p_x, t)$:

$$\frac{\partial f}{\partial t} + \frac{p_x}{\gamma m}\frac{\partial f}{\partial x} - e(E_x + u_y B_z)\frac{\partial f}{\partial p_x} = 0, \tag{1}$$

where $\gamma = (1 + p_x^2/m^2c^2)^{1/2}$ and $p_x = m\gamma u_x$. We shall restrict attention to time-scales that are short compared to the ion plasma period, so that the ions are taken to be immobile. Indeed, in our simulations, we typically study electron dynamics over a time $t = 200\omega_{pe}^{-1}$, which is $t \simeq 4.6\omega_{pi}^{-1}$, if $m_i/m_e = 1836$ (proton to electron mass ratio). The transverse velocity u_y, generated by the electromagnetic field of the laser, is nonrelativistic and obeys

$$\frac{\partial u_y}{\partial t} = -\frac{e}{m}E_y. \tag{2}$$

This expresses conservation of the transverse canonical momentum $p_y = u_y - (e/m)A_y$, with $E_y = -\partial A_y/\partial t$. Relativistic effects are fully taken into account in the longitudinal direction, which is the direction of acceleration of the electrons. However, in equation (2), which governs the transverse dynamics, the Lorentz factor γ has been neglected. This

https://doi.org/10.1017/S0263034600010880 Published online by Cambridge University Press

assumption does not affect the evolution in any appreciable way. The reason is that the coupling between the longitudinal and transverse directions (which is the crucial nonlinear effect) is largely dominated by the cold background population of electrons, for which $\gamma \simeq 1$. For the electrons participating in the plasma wave, $\gamma > 1$, and it should in principle be included in the equations: however, the resulting correction is negligible, because the longitudinal force eE_x is much larger than the Lorenz force $eu_y B_z$. In other words, the term $eu_y B_z$ needs to be treated to high accuracy only for the cold electrons, for which $\gamma = 1$ is a good approximation. This assumption was used by Bertrand *et al.* 1994.

The longitudinal electric field is obtained self-consistently from Poisson's equation,

$$\frac{\partial^2 \phi}{\partial x^2} = -\frac{e}{\epsilon_o}\,[n_i(x) - n_e(x,t)], \tag{3}$$

with $n_e = \int f\, dp_x$ and $E_x = -\partial\phi/\partial x$. The transverse electromagnetic fields obey Maxwell's equations,

$$\frac{\partial B_z}{\partial t} = -\frac{\partial E_y}{\partial x} \tag{4}$$

$$\frac{\partial E_y}{\partial t} = -c^2 \frac{\partial B_z}{\partial x} - \frac{1}{\epsilon_o} J_y, \tag{5}$$

$$J_y = -e n_e(x,t) u_y(x,t)$$

which can be written more conveniently in terms of the forward and backward electromagnetic fields $E^{\pm} = E_y \pm cB_z$:

$$\left(\frac{\partial}{\partial t} \pm c\frac{\partial}{\partial x}\right) E^{\pm} = -\frac{1}{\epsilon_o} J_y. \tag{6}$$

The preceding equations constitute our mathematical model. Most numerical codes for the Vlasov equation (1) rely on particle-in-cell (PIC) techniques: a large number of particles are advanced along the characteristics of the Vlasov equation, and the electron density is reconstructed at each time step to solve the Poisson equation. The major drawback of PIC techniques lies in the fact that, often, the most interesting phenomena occur in regions of phase space where the number of particles is very small, and resolving coherent structures becomes a difficult task.

Here, we shall make use of an Eulerian Vlasov code (Ghizzo *et al.* 1993), which is described in more detail in the Appendix. In Eulerian codes, the entire phase space is covered with a uniform mesh, and the Vlasov equation is solved by means of a splitting scheme, which alternately advances the distribution function in the x and in the p_x directions. These codes allow very fine resolution in phase space even in regions where the electron density is low, as for example in the extended tail of an energetic electron distribution function.

3. Numerical results

In this section, we make use of the numerical code previously described to simulate the interaction of laser light with an underdense plasma. By writing the pertinent equations in a dimensionless form, three dimensionless quantities appear to play a crucial role: ω_o/ω_p, the ratio of laser to plasma frequency; $v_{\rm th}/c$, the electron thermal velocity; and $v_{\rm osc}/c = eE_o/m\omega_o c$, the "quiver" velocity, where E_o is the laser electric field. In the simulations that we will present, these parameters take the values $\omega_o/\omega_p = 3.35$, $v_{\rm osc}/c = 0.239$ and $v_{\rm th}/c = 0.09$. The corresponding value of k_o is $3.2\omega_p c^{-1}$.

https://doi.org/10.1017/S0263034600010880 Published online by Cambridge University Press

Furthermore, a small fraction α of the electron population commences the simulation with a higher temperature T_{hot}. Such a hot population can be created by the interaction of the plasma with the laser itself, as was indeed observed in some experiments (Aithal *et al.* 1987). A possible mechanism, as suggested in the introduction, could be SCS.

The total length of the plasma is $L = 120\lambda_o = 255.25c\omega_p^{-1}$, where $\lambda_o = 2\pi/k_o$ is the laser wavelength, and k_o satisfies $\omega_o^2 = \omega_p^2 + c^2k_o^2$. The background density profile is plotted in figure 1: this represents the density of the immobile ions as well as the initial electron density. A region of vacuum occupying a length $L_{\text{vac}} = 5\lambda_o$ is present at both sides of the plasma.

The initial condition for the distribution function is:

$$f(x, p_x, t = 0) = n_i(x)F_o(p_x) \tag{7}$$

$$F_o(p_x) = \frac{(1-\alpha)}{\sqrt{2\pi m T_{\text{cold}}}} \exp\left(-\frac{p_x^2}{2mT_{\text{cold}}}\right) + \alpha A \exp\left(-\frac{mc^2(\gamma - 1)}{T_{\text{hot}}}\right), \tag{8}$$

where $\alpha = 0.05$, and A is a constant chosen so that $\int F_o\, dp_x = 1$.

If we assume a plasma density $n \sim 10^{20}$ cm^{-3}, the dimensionless parameters introduced above correspond to the following dimensional values: $T_{\text{cold}} = 4.1$ keV, $T_{\text{hot}} = 31.6$ keV corresponding to a characteristic velocity $0.24c$ for the small hot fraction, $\omega_p = 5.7 \times 10^{14}$ s^{-1}, $\lambda_o = 1.03$ μm and $\omega_o = 2 \times 10^{15}$ s^{-1}. The laser intensity $I_o = \epsilon_o E_o^2 c/2$ takes the value 7.7×10^{16} Wcm^{-2}. Two simulations are presented, the first with a flat density profile as illustrated in figure 1, and the second with a small density gradient such that $\lambda_o|\nabla n/n| \ll 1$.

In figure 2, the momentum distribution function, averaged over different spatial regions, is plotted at different times. The hot electron tail is most pronounced for $L/4 < x < L/2$ (figure 2b) because when the plasma wave enters this region, it has almost reached its maximum amplitude, so that the electrons can be accelerated with high efficiency. The region $0 < x < L/4$ (figure 2a) is crossed by the plasma wave when it is still growing and, for the times considered here, the wave has hardly had the time to penetrate into the region $L/2 < x < 3L/4$ (figure 2c): this explains the smaller number of accelerated electrons in these regions. The maximum electron energy is roughly 7 MeV. Note that in the simulations we normalize time to ω_p^{-1}, space to $c\omega_p^{-1}$ and momentum to mc: this is reflected in the captions to all subsequent figures. We also note that, for ultrarelativistic electrons, $E/mc^2 = p/mc$, and $mc^2 \simeq 0.5$ MeV, where m is the electron rest mass. The value of 7 MeV

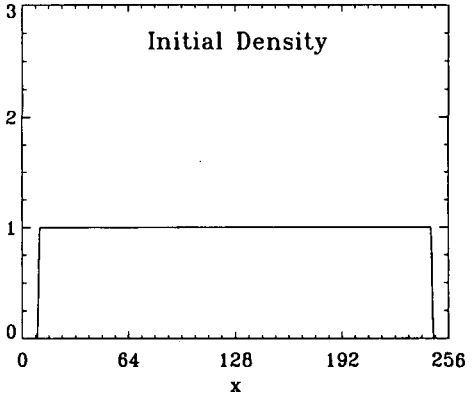

FIGURE 1. Initial electron density profile for the first simulation.

https://doi.org/10.1017/S0263034600010880 Published online by Cambridge University Press

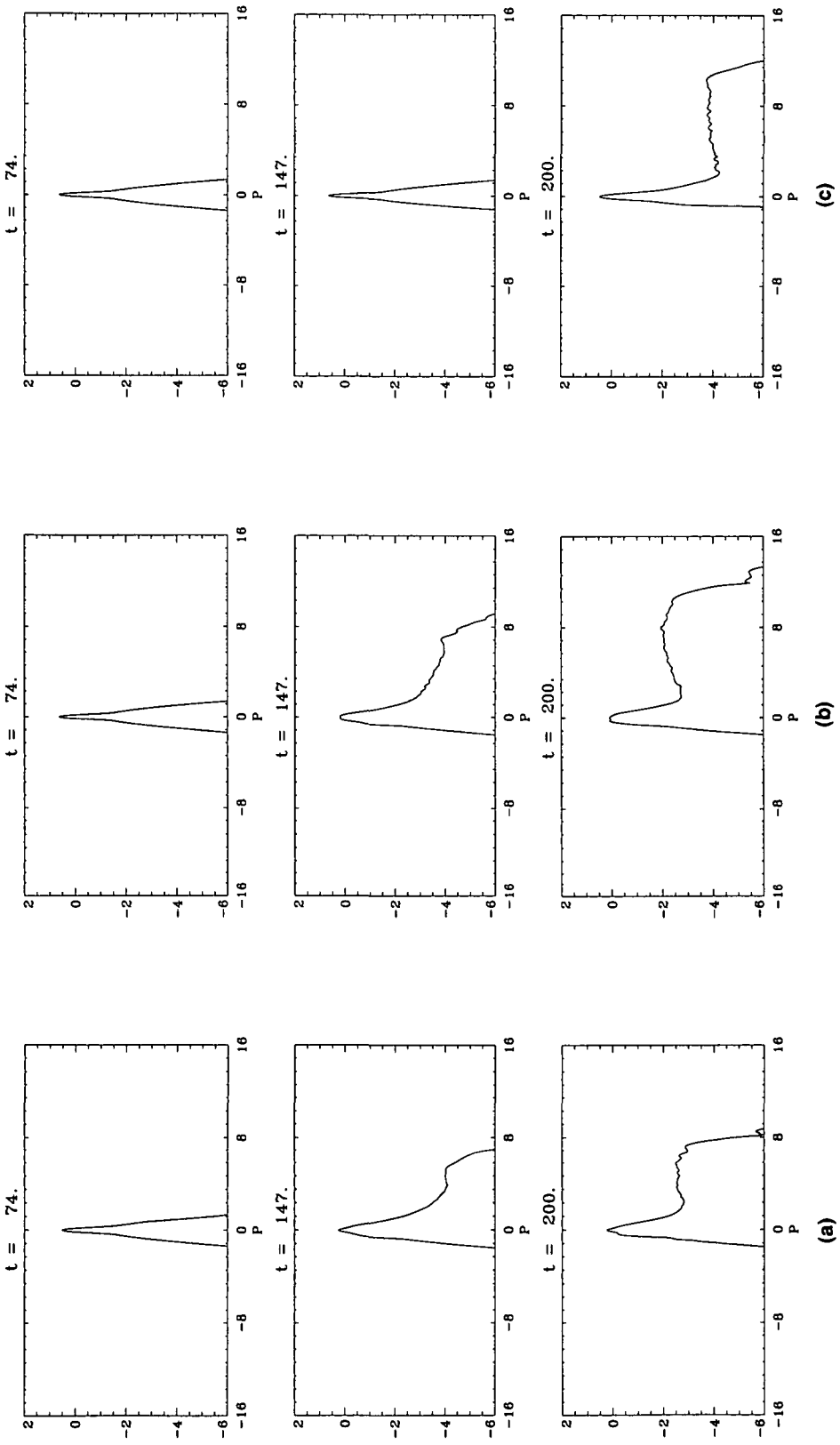

FIGURE 2. Longitudinal momentum distribution function averaged over three spatial regions: (a) $0 < x < L/4$; (b) $L/4 < x < L/2$; and (c) $L/2 < x < 3L/4$. Three different times are shown: $\omega_p t = 74$ (top frame); $\omega_p t = 147$ (middle frame); and $\omega_p t = 200$ (bottom frame). Momentum is measured in units of mc, where m is the electron rest mass. To convert to energy units, recall that $mc \simeq 0.5$ MeV/c.

https://doi.org/10.1017/S0263034600010880 Published online by Cambridge University Press

is significant, since it is the threshold energy for generating bremsstrahlung photons of sufficient energy to extract a neutron from its nucleus (photoneutron production). The fraction of electrons accelerated to multi-MeV energies is typically 1% of the total population.

Snapshots of the electrostatic and electromagnetic fields at various times are shown in figure 3. The electrostatic field grows linearly in the first part of the simulation, up to $\omega_p t \simeq 150$: this results in a neat wave-packet with wave number k_p, traveling at its group velocity. At subsequent times, nonlinear effects cause saturation of the instability, and the plasma wave develops a more complex structure with a broader wave number spectrum. The saturation mechanism can be due to the detuning of the plasma wave by two main effects: density depletion induced by the wave itself and relativistic increase of the electron mass, both leading to a modification of the local plasma frequency. Saturation could also arise from electron trapping by the plasma wave, or wave breaking. Note that we have suppressed the component of the E^+ field corresponding to the pump wavenumber k_o (equal to $3.2\omega_p c^{-1}$ in our case), so that the residual E^+ represents the Stokes and anti-Stokes waves with wave numbers $k_o \pm k_p$ (see also figure 4). From figures 3b and 3c (bottom frame), we note that the anti-Stokes wave $(k_o + k_p)$ is localized in the front of the packet, while the Stokes wave $(k_o - k_p)$ is localized in the rear. E^-, the electromagnetic field traveling backwards, develops a long wavelength structure around saturation, more clearly seen in wave number space (figure 4). Using the dimensionless parameter set described above, the Stokes, anti-Stokes and respective plasma waves have wave numbers, for the SRFS case: $k_S \simeq 2.12\omega_p/c$, $k_p = k_o - k_S \simeq 1.07\omega_p/c$, $k_{AS} \simeq 4.23\omega_p/c$; and $k_p' = -k_o + k_{AS} \simeq 1.03\omega_p/c$. The Stokes and anti-Stokes components are visible as sidebands of the pump wave in the spectrum of the forward electromagnetic field E^+. Their respective plasma waves are almost superposed at $k_p \simeq \omega_p c^{-1}$. Other modes with $k \simeq \omega_p c^{-1}$ and $k \simeq 5\omega_p c^{-1}$ are visible in the E^+ spectrum at later times, and these originate from nonlinear couplings of k_S and k_{AS} with the plasma wave.

The spectrum of E^- is more difficult to interpret: we observe excitation at wave numbers similar to those of E^+, but in E^- modes with a smaller wave number are more strongly excited. The mode $k \simeq 2\omega_p c^{-1}$ could be due to SRBS, for which we have $k_S \simeq 2.12\omega_p c^{-1}$ and $k_p = k_o - k_S \simeq 5.3\omega_p c^{-1}$ (the sign of k_S is irrelevant, because $E_{-k} = E_k^*$, E being a real quantity). The corresponding plasma wave is strongly damped, because $k_p \lambda_D \simeq 0.48$, and thus does not appear in the spectrum. The time evolution of the E^- spectrum shows that the mode $k \simeq 3\omega_p c^{-1}$ appears first, followed by $k \simeq 2\omega_p c^{-1}$ and finally $k \simeq \omega_p c^{-1}$. We suggest that the mode $k \simeq 3\omega_p c^{-1}$ comes from the coupling between the pump wave k_o and a strongly damped plasma wave $k_p' = 2k_o$ arising from Compton scattering, which gives rise to a scattered wave

$$k_S = k_o - k_p' \approx -k_o = -3.2\omega_p c^{-1}. \tag{9}$$

This scattered wave is the one observed in the E^- spectrum. This process can also be viewed as the partial reflection of the pump wave: the incident (k_o) and reflected $(-k_0)$ waves then combine to produce a plasma wave with wave number $k_p' = 2k_o = 6.4\omega_p c^{-1}$, which is strongly Landau damped, because $2k_o\lambda_D \simeq 0.58$. To check our hypothesis, we have repeated the simulation with a lower electron temperature ($v_{\text{th}} = 0.02c$) to reduce the efficiency of Landau damping. In this case $2k_o\lambda_D \simeq 0.13$, and a plasma wave at $k_e = 2k_o$ is indeed observed very early in the evolution, as shown in figure 4d.

Once the scattered wave $k_S = -k_o$ has been created, it couples to the plasma wave $k_p \simeq \omega_p c^{-1}$ to excite the mode $k \simeq 2\omega_p c^{-1}$. In a similar way this mode couples again with the plasma wave to give rise to the mode $k \simeq \omega_p c^{-1}$. At each step of this cascade, the amplitude of the electromagnetic wave grows larger because it couples to a plasma wave with higher amplitude. This is the opposite of what happens in the ordinary Stokes and

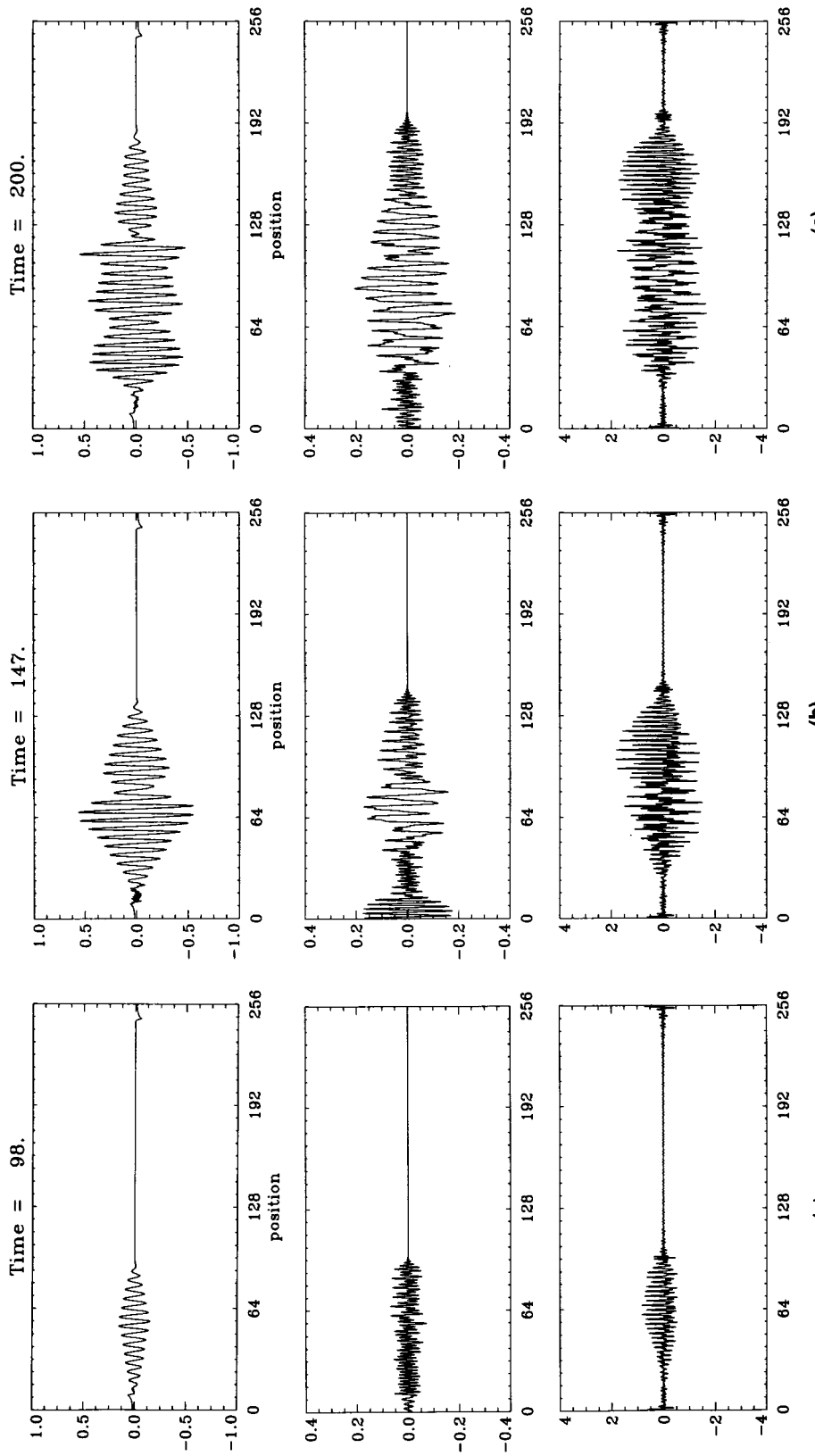

FIGURE 3. Electrostatic field (top frame), backscattered field E^- (middle frame) and forwardscattered field E^+ (bottom frame) as a function of dimensionless position $\omega_p^{-1}cx$, at times (a) $\omega_p t = 98$; (b) $\omega_p t = 147$; and (c) $\omega_p t = 200$. In the E^+ field the component corresponding to the pump wave has been suppressed.

https://doi.org/10.1017/S0263034600010880 Published online by Cambridge University Press

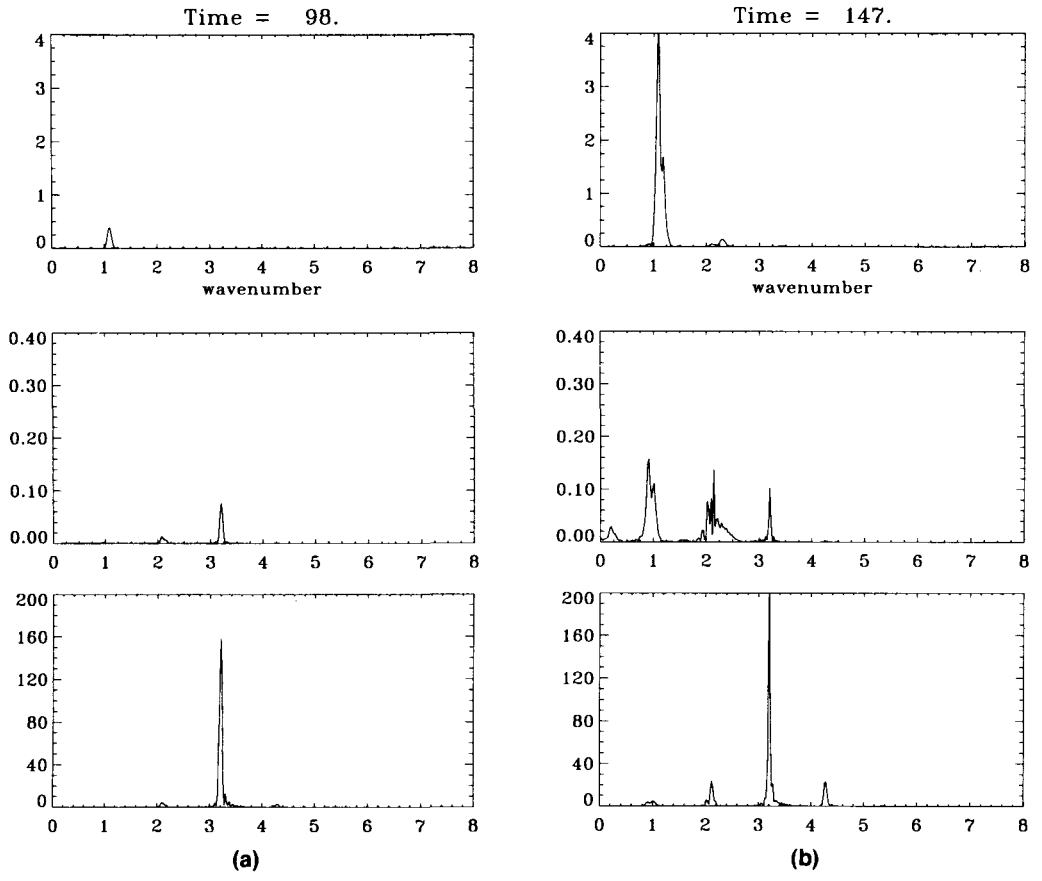

FIGURE 4. Squared modulus of the electrostatic field (top frame), backscattered field E^- (middle frame) and forwardscattered field E^+ fields (bottom frame) in wave number space (units are $\omega_p c^{-1}$), at times (a) $\omega_p t = 98$; (b) $\omega_p t = 147$. (See p. 205 for continuation of figure 4.)

anti-Stokes processes, in which the scattered wave has a smaller amplitude than the pump wave.

In figure 5 we show the time history of the electrostatic field at two different points in space. The dominant frequency $\omega_e = (\omega_p^2 + 3v_{\rm th}^2 k_e^2)^{1/2}$ is clearly visible. For $x = L/4$ (figure 5a), saturation occurs at $\omega_p t \simeq 150$; then a much slower modulation appears, with $\omega \simeq 0.08\omega_p$. The plasma wave arrives at $x = L/2$ (figure 5b) after saturation has already occurred, so that no further growth is visible. The same pattern is observed in the time evolution of the spatially integrated electrostatic and kinetic energies, shown in figure 6a. In figure 6b the electrostatic energy is plotted on a logarithmic scale (in base 10) to evaluate the growth rate of the instability. In the initial evolution, two stages are clearly visible, beginning at $\omega_p t \simeq 10$ and $\omega_p t \simeq 60$, with growth rates, respectively, $\gamma_1 \simeq 0.016\omega_p$ and $\gamma_2 \simeq 0.029\omega_p$. At $\omega_p t \simeq 150$ the growth has saturated. A simple analytical estimate (Mori 1994), which neglects the electron temperature, gives the following growth rate, for a typical quadratic quantity such as the energy:

$$\gamma = \sqrt{2}\left(\frac{\omega_p}{\omega_o}\right)^2 \frac{v_{\rm osc}}{c}\,\omega_p \tag{10}$$

https://doi.org/10.1017/S0263034600010880 Published online by Cambridge University Press

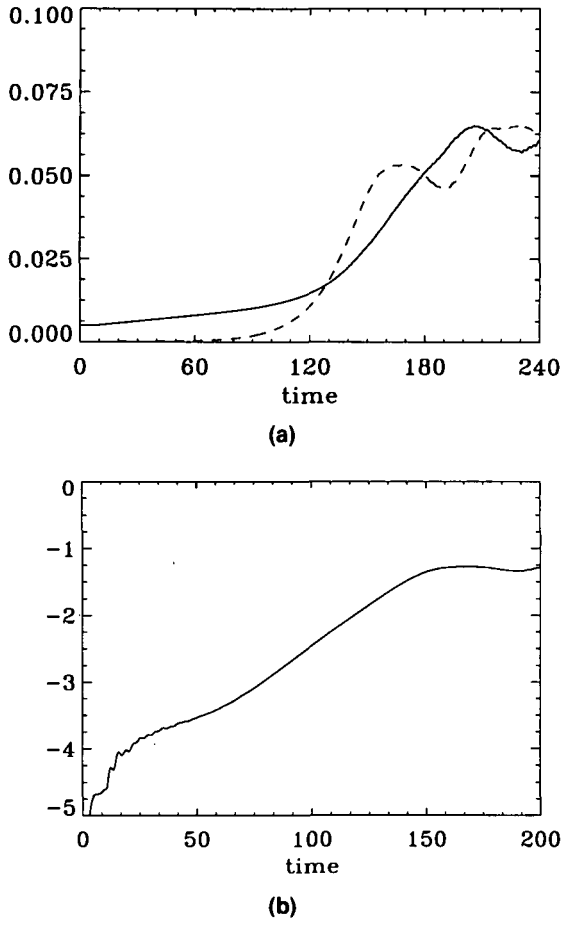

FIGURE 6. (a) Time history of the kinetic energy (solid line) and of the electrostatic energy (times a factor four, broken line), both integrated over the whole plasma length. (b) Time history of the electrostatic energy on a log scale in base 10.

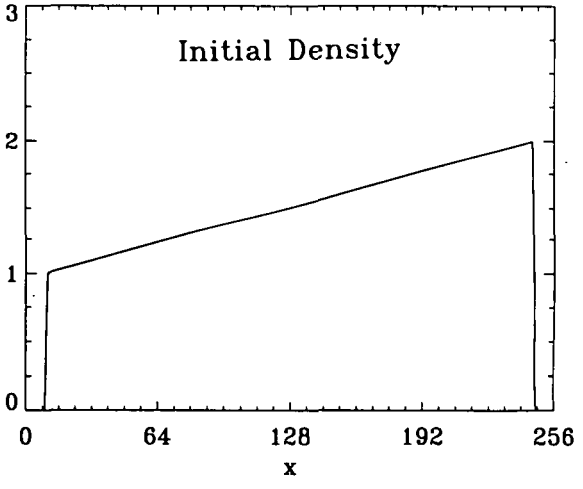

FIGURE 7. Initial electron density profile for the second simulation.

https://doi.org/10.1017/S0263034600010880 Published online by Cambridge University Press

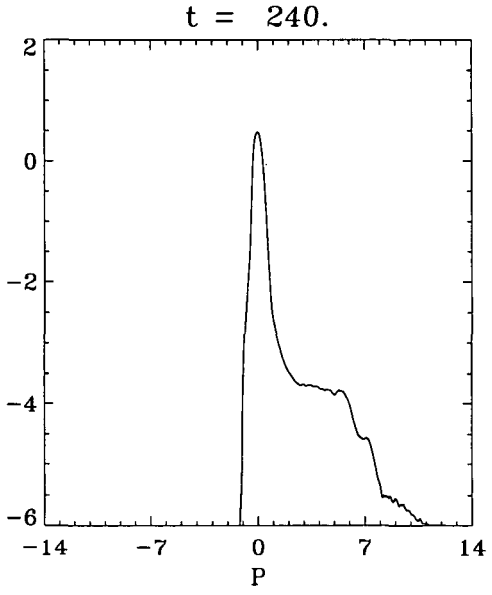

FIGURE 8. Longitudinal momentum distribution function averaged over the region $L/2 < x < 3L/4$ at the end of the simulation ($\omega_p t = 240$).

ments. Numerical simulations have been performed in a range of parameters comparable to those of laser plasma experiments (Modena *et al.* 1995). In our case, the electron temperature is 3 keV, $\omega_o/\omega_p = 3.35$ and $I_o = 7.7 \times 10^{16}$ W cm^{-2}. The results show that a high energy tail of multi-MeV electrons is indeed created as a result of stimulated Raman scattering. These energetic electrons can emit photons through bremsstrahlung, which in turn may be responsible for photoneutron production.

Our simulations have shown, for the first time to our knowledge, the development of stimulated Compton scattering at a very early stage of the laser–plasma interaction. Stimulated Compton scattering generates a plasma mode with wave number of $2k_o$, which, however, is strongly Landau damped (in our case $2k_o\lambda_D = 0.58$). Therefore, the corresponding plasma wave cannot develop, and the energy is directly transferred to thermal electron motion (this is often referred to as a "quasi-mode"). Although, in our simulation, a high-temperature component of the electron population was already present as an initial condition, stimulated Compton scattering could provide an efficient mechanism for preheating the plasma, thus improving the efficiency of the forward Raman instability in electron energization. In our case, the laser is so intense that it can extract the electrons directly from the hot tail ($T_{\text{hot}} = 31.6$ keV) and accelerate them to ultrarelativistic velocities. Energies up to 7 MeV have been observed in the simulation.

The analysis of the electromagnetic spectrum has been particularly interesting. While the forward electromagnetic field reveals the expected Stokes and anti-Stokes sidebands at $k_o \pm \omega_p c^{-1}$, the backward field possesses a more complex structure. This structure has been interpreted as a cascade originating, in the first place, from a Compton backscattered wave, which couples to the plasma wave giving rise to another backscattered light wave with a smaller wave number, and so forth. This long wavelength pattern is localized well inside the bulk of the plasma, and does not seem to propagate toward the boundary.

Finally, we have investigated the same problem in the presence of a small density gradient in the plasma profile. The result is that the electrons are accelerated to lower energies

https://doi.org/10.1017/S0263034600010880 Published online by Cambridge University Press

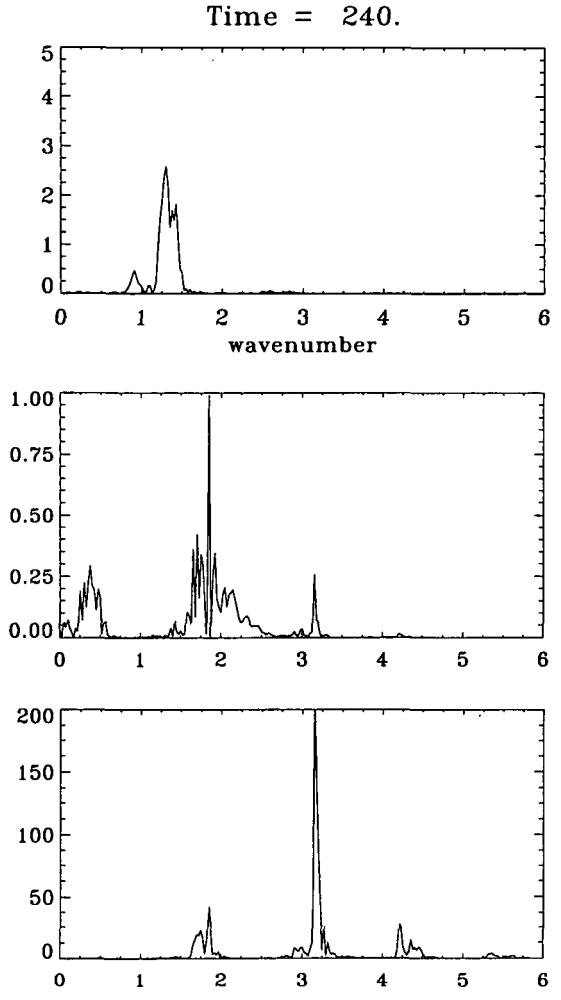

FIGURE 9. Squared modulus of the electrostatic field (top frame), E^- (middle frame) and E^+ (bottom frame) fields in wave number space at $\omega_p t = 240$.

(~3.5 MeV), because the plasma is globally less under-critical than in the previous case. Also, the plasma frequency now being a function of position, we have observed a shift of wave number in the electrostatic and electromagnetic spectra.

As a concluding remark, we note that our simulations suggest that non-negligible production of high-energy electrons can be expected in the range of physical parameters considered. The numerical code that we have used is a potentially valuable tool in investigating possible configurations for indirect drive laser fusion experiments, hopefully reducing the number of accelerated electrons.

Acknowledgments

The authors wish to thank E. Fijalkow, M. Shoucri, A. Ghizzo, and P. Bertrand for providing the numerical code. This work was supported in part by the Commission of the European Communities under Contract Nos. ERBCHBICT941009 and ERBCHRXCT940604.

REFERENCES

AITHAL, S. *et al.* 1987 *Phys. Fluids* **30**, 3832.
BERTRAND, P. *et al.* 1994 *Phys. Rev. E* **49**, 5656.
DECKER, C.D. *et al.* 1994 *Phys. Rev. E* **50**, 3338.
EVERETT, M.J. *et al.* 1995 *Phys. Rev. Lett.* **74**, 1355.
GHIZZO, A. *et al.* 1993 *J. Comp. Phys.* **108**, 105.
JOSHI, C. *et al.* 1984 *Nature* **311**, 525.
KRUER, W.L. 1988 *The Physics of Laser Plasma Interactions* (Addison-Wesley, Redwood City, CA).
LIN, A.T. & DAWSON, J.M. 1975 *Phys. Fluids* **18**, 201.
MCKINSTRIE, C.J. & BINGHAM, R. 1992 *Phys. Fluids B* **4**, 2626.
MODENA, A. *et al.* 1995 *Nature* **377**, 606.
MORI, W.B. 1994 *Physica Scripta* **T52**, 28.
OFFENBERGER, A.A. *et al.* 1982 *Phys. Rev. Lett.* **49**, 371.
TABAK, M. *et al.* 1994 *Phys. Plasmas* **1**, 1626.

APPENDIX: THE NUMERICAL CODE

Vlasov Eulerian codes are based on a splitting scheme which, for the present case, involves three main steps:

Step 1: Between t_n and $t_{n+1/2}$ shift the distribution function in x-space for a time $\Delta t/2$

$$f^*(x, p_x, t_{n+1/2}) = f\left(x - \frac{p_x}{m\gamma}\frac{\Delta t}{2}, p_x, t_n\right). \tag{A1}$$

Step 2: Compute the fields at time $t_{n+1/2}$, then shift the distribution function in p_x space for a time Δt.

$$f^{**}(x, p_x, t_{n+1/2}) = f^*(x, p_x + e\Delta t(E_x + u_y B_z), t_{n+1/2}). \tag{A2}$$

Step 3: Between $t_{n+1/2}$ and t_n shift again in x-space for a time $\Delta t/2$

$$f(x, p_x, t_{n+1}) = f^{**}\left(x - \frac{p_x}{m\gamma}\frac{\Delta t}{2}, p_x, t_{n+1/2}\right). \tag{A3}$$

This scheme enables us to compute the distribution function at time t_{n+1}, when its value at time t_n is known. It is correct to second order in Δt. To perform the shifts, we need an interpolation technique, which is provided by a cubic spline method.

Furthermore, when performing Step 2, we require knowledge of the electromagnetic fields. To obtain the longitudinal electrostatic field, the Poisson equation is solved via a cubic spline scheme, correct to order Δx^4. The Maxwell equations (4) and (5) are solved between $t_{n-1/2}$ and $t_{n+1/2}$ using a time-centered scheme:

$$E^{\pm}(x + c\Delta t, t_{n+1/2}) - E^{\pm}(x, t_{n-1/2}) = -\frac{\Delta t}{\epsilon_o} J_y\left(x \pm c\frac{\Delta t}{2}, t_n\right). \tag{A4}$$

Choosing a time step such as $\Delta x = c\Delta t$ allows us to advance equation (5) exactly, provided an interpolation for the right hand side is given. We have chosen the following scheme to interpolate J_y along the vacuum characteristics:

$$J_y\left(x \pm \frac{\Delta x}{2}, t_n\right) = -\frac{e}{2}\left[n_e(x \pm \Delta x, t_{n+1/2})u_y(x \pm \Delta x, t_n) + n_e(x, t_{n-1/2})u_y(x, t_n)\right]. \tag{A5}$$

https://doi.org/10.1017/S0263034600010880 Published online by Cambridge University Press